UNIVERSITY OF WATERLOO

Department of Mechanical and Mechatronics Engineering

ME362 - Fluid Mechanics 2
Project 2 - The Fluid Mechanics of An Arrow

Prepared For:
Professor Serhiy Yarusevych

Prepared By:
Zeshan Qureshi
Samuel Street
Nam Tran
David Wheatle

University of Waterloo
200 University Ave. West
Waterloo, Ontario, N2L 3G1

Date:
December 4th, 2023

Contents

1 Introduction

1.1 Physics of Archery

First introduced to the Olympic games in year 1900, archery is one of the oldest sports still practiced today [1]. In its simplest form, archery is practiced using a bow and arrow. The archer first places their arrow in the direction they want to shoot, ensuring it is perpendicular to the string of the bow. Then, the archer pulls the bow back against the resistance of the bow string. Once the bow string begins to feel tight, the archer will release the bow string. Figure 1 shows the stance archers use before shooting an arrow.

Figure 1: Archer Pulling Back Bowstring [2]

The tension in the string propels the arrow in the air. For an arrow gliding towards its target, a snapshot can be taken to analyze the forces acting on the arrow. Figure 2 below shows the forces acting on the arrow as it glides in the air.
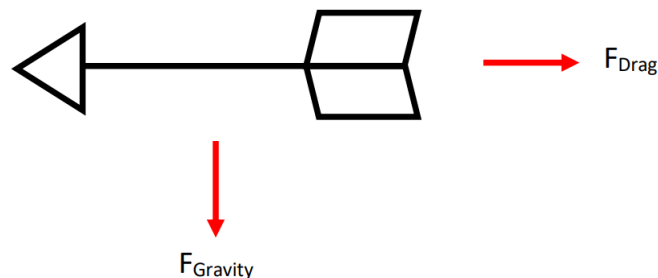

Figure 2: Forces on an Arrow

In this diagram it can be seen that the main forces acting on the arrow are drag and gravity. In the next section, the drag force will be further broken down into its components and fluid analysis will be performed to help develop a model to visualize the flow.

1.2 Background Information

This report will describe the process to model fluid flow over an arrow. All fluids in motion can be represented by streamlines. Streamlines are defined as lines that are tangent to the local velocity vector at a given instant in time [3]. Streamline functions (ψ) are mathematical equations that represent the streamline of a

fluid. By definition, the velocity field of the fluid is the curl of the streamline function ($\overrightarrow{V} = \nabla \times \psi$) and is defined in a way that it satisfies the continuity equation. In order for the streamline function to exist, the velocity field must satisfy the continuity equation ($\frac{dv}{dx} - \frac{dv}{dy} = 0$) [4]. The velocity potential (ϕ) is another visualization method used to describe fluid flow. By definition, the velocity field of the fluid is the gradient of the velocity potential function ($\overrightarrow{V} = \nabla\phi$) and is defined in a way that it satisfies the irrotionality condition. In order for the velocity potential function to exist, the velocity flow must satisfy the irrotationality condition ($\nabla \times \overrightarrow{V} = 0$) [4].

There are a few basic potential flow solutions that can be used to model real systems. The first solution is uniform flow and it represents flow that remains unchanged over time (unless acted upon by an external force). Figure 3 below represents uniform flow for velocity in the i-direction [5].
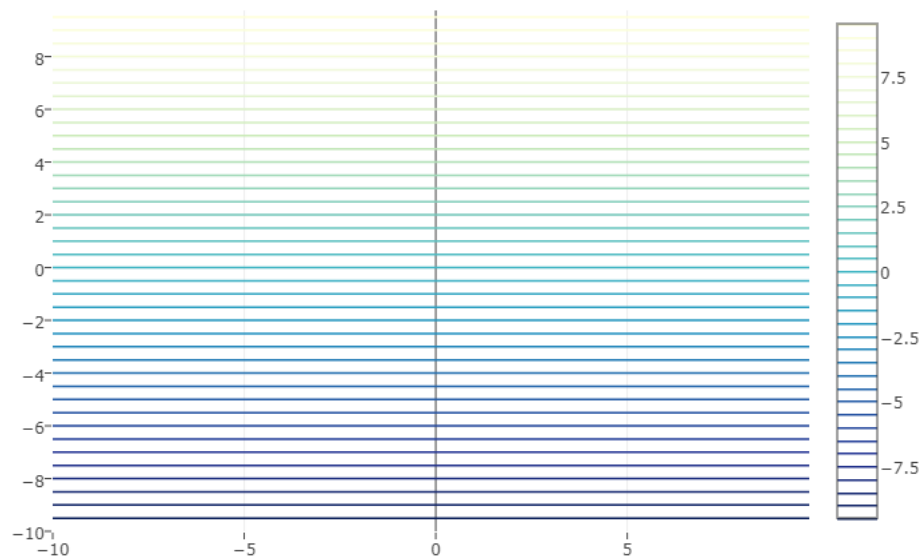

Figure 3: Uniform Flow Solution

The streamline equation for the uniform flow solution above can be found below.

$$\psi(x, y) = -Vx + Uy$$
$$U = 1$$
$$V = 0$$
$$\psi(y) = y$$

The next solution is a source model and it represents a solution where the fluid streamlines flow radial outwards away from the center of a circle. For the source solution, circles of varying diameter that are centered at the source represent velocity potentials (ϕ) that are constant. Figure 4 below shows the generalized source solution [5].
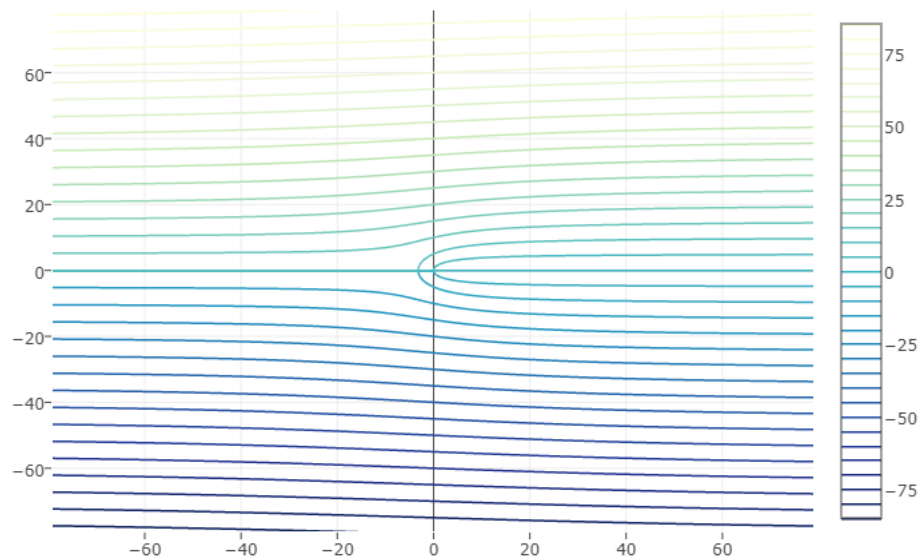
Figure 4: Source Solution

The streamline equation for the source solution above can be found below. Since streamline functions are described using the Laplace equation, the uniform flow solution above can be added to the point source solution equation using the superposition method.

$$\psi_{\text{source}}(x, y) + \psi_{\text{uniform}}(y) = (\frac{m}{2\pi} \tan^{-1}(\frac{y - y_0}{x - x_0})) + (y)$$

$$m_{\text{strength}} = 20$$

$$x_0 = 0$$

$$y_0 = 0$$

$$\psi(x, y) = \frac{20}{2\pi} \tan^{-1}(\frac{y}{x}) + y$$

The next solution is a sink model and it represents a solution where the fluid streamlines flow radial inwards towards the center of a circle. For the sink solution, circles of varying diameter that are centered at the sink represent velocity potential (ϕ) equations that are constant. Figure 5 below shows the generalized sink solution [5].
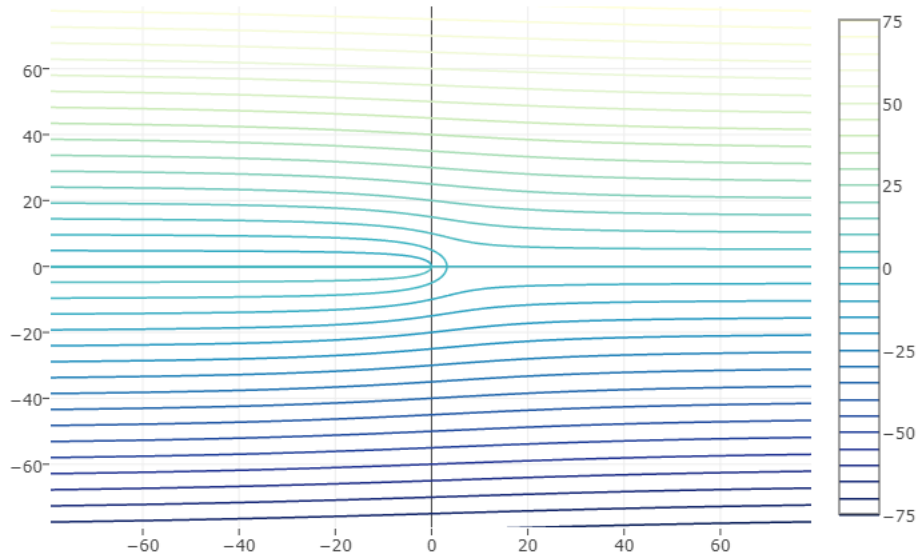
Figure 5: Sink Solution

The streamline equation for the sink solution above can be found below. Similar to the approach above, the superposition method can be used to add the uniform flow solution.

$$\psi_{\text{sink}}(x, y) + \psi_{\text{uniform}}(y) = (\frac{-m}{2\pi} \tan^{-1}(\frac{y - y_0}{x - x_0})) + (y)$$

$$m_{\text{strength}} = -20$$

$$x_0 = 0$$

$$y_0 = 0$$

$$\psi(x, y) = -\frac{20}{2\pi} \tan^{-1}(\frac{y}{x}) + y$$

One of the fundamental relationships of fluid analysis is the Navier-Stokes equation. In simple terms, the Navier-Stokes equation represents Newton's second law of motion. On the left hand side of the equation, we have mass times acceleration ($\rho \times \frac{du}{dt}$). On the right side of the equation, the force components are due to the pressure gradient, viscosity, and gravity [6]. The Navier-Stokes equation can be represented in all three axis but for simplicity, the equation below shows the Navier-Stokes equation for the x-direction.

$$\rho(\frac{du}{dt} + u\frac{du}{dx} + v\frac{du}{dy} + w\frac{du}{dz}) = -\frac{dP}{dx} + \mu(\frac{d^2u}{dx^2} + \frac{d^2u}{dx^2} + \frac{d^2u}{dy^2} + \frac{d^2u}{dz^2}) + g_x$$

Since the Navier-Stokes equation is difficult to solve, practical engineering analysis allows for the use of appropriate approximations within different regions of flow. In the inviscid regions of flow, where viscous effects are deemed to be negligible, the Navier Stokes equation can be reduced to the Euler equation. In the inviscid region of flow, Euler's equation can be used to derive the Bernoulli equation, which is valid along streamlines of flow.

4

The application of potential flow and Euler's equation is limited to regions of negligible viscosity and cannot be applied to regions of no slip boundary regions, such as areas where fluid flows over a contacting surface. This is where the boundary layer assumptions can be applied. The boundary layer specifically refers to the thin layer of flow in which viscous effects and vorticity are significant.The boundary layer approximation is appropriate for high Reynolds number and in regions near the wall, wakes, jets and mixing layers. In our evaluation of the boundary layer thickness, the specific parameters that characterize the boundary layer include the boundary layer thickness, the displacement thickness and the momentum thickness.

As the Reynolds number of fluid flow increases as it moves along the length of a wall, the flow transitions from laminar to turbulent flow, As turbulent flow is inherently unsteady and the instantaneous velocity profile varies with time, the boundary layer equations cannot be solved for turbulent flow

For the purpose of the boundary layer analysis carried out in this report, the Momentum Integral equation, developed by Theodore von Karman (1881-1963) is valid for both laminar and turbulent boundary layers that are exposed to arbitrary nonzero pressure gradients.

Some of the variables that affect the flow of a fluid are velocity, viscosity, and density. The geometry and smoothness of the surface that the fluid flows over also plays a role in the fluid flow.

2   Objective

The objective of the project is to identify the most stable arrow shape for long distance shooting through implementing numerical model in Matlab to identify the boundary layer and force exerted on the model , moment about he arrow and how stability and restoring force changes with arrow length, fin shape and arrow head shape.

3   Methodology

3.1   Assumptions

In determining the appropriate assumptions to simplify the modelling efforts that need to be completed, it was first necessary to limit the scope of this analysis to 2D flow. Although there is nominally a 3rd or 4th fin, this would be hard with potential flow modelling. Additionally, it has been assumed that the flow across the arrow is in steady state to allow the use of potential flow. The external flow is also assumed to be inviscid and in-compressible and that the boundary layer grows small enough such that the surface streamline does not interfere with the body streamline. It is assumed that the velocity at the outer layer of the boundary layer is equivalent to the velocity from the potential flow model about the body streamline.

Aside from other common assumptions, it is additionally assumed for this analysis that any additional fins outside of this 2D plane do not affect the flow across the fins under consideration. Additionally, to be steady state, it is assumed that the rigid body of the arrow projectile does undergo dynamic behaviour.

3.2   Identification of Arrow Dimensions Parameter

In this study, the length of the arrow is defined to be 27 inch and the diameter of the arrow is approximately to be 1 inch according to [7]. As mentioned in objective, since the goal is to identify the best fin for the arrow, the following list of fin types will be the focus in this study. These fins were obtained from standard fin geometries that are typically used [8] .

- Old English FS

- Old English SL

- Shield

- Pope & Young

- French Curve

To further simplify the study, the dimension for each find type will be standardized, therefore, the length and height of fin is 6 in and 2 in, respectively as shown below.
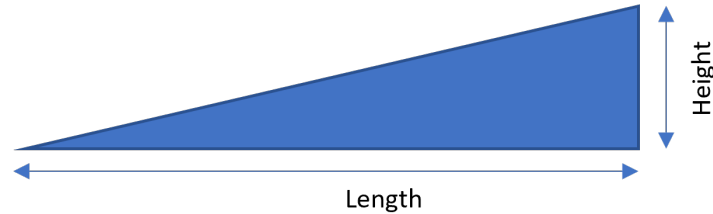

Figure 6: Arrow Fin Size Standardization

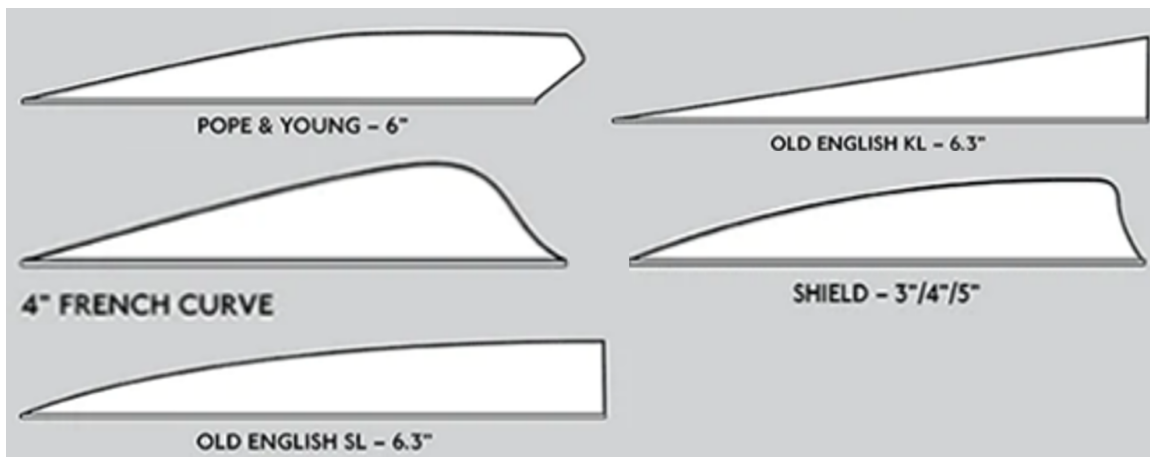The Figure 7 below will show the expected shape of the arrow fin shape.

Figure 7: Arrow Fin Shape [8]

4   Model Development

Given a desire to produce a simplified model with geometry similar to that of the arrow, as previously described in section 3, an initial model consisting of basic flow components was attempted. Given the long flat main length of the arrow, following the leading cap and before the fin of the arrow, this region would need to be modelled with great accuracy to ensure that the flow passing over the fins are as close to the realistic value as possible. To simulate this region, it was initially envisioned that a doublet sheet, essentially replicating the use of a vortex sheet in that it can produce a almost horizontal flow close to the vortex boundaries, but in this case would produce flow towards the rightmost quadrants both above and below the sheet. The elliptical forward and reverse caps match a similar profile to the halves of the Rankine

half-body, and were thus considered or use in producing the desired geometry when connecting to the doublet sheet. As such, the use of Equation 1 would need to be repeated in addition to the use of Equation 2 with an appropriate sign of m to act as the source and sink respectively [9, pg.537].

$$\psi = \lim_{a \to 0} \left(-m \arctan \frac{2ay}{x^2 + y^2 - a^2} \right) = -\frac{2amy}{x^2 + y^2} = -\frac{\lambda y}{x^2 + y^2}, \quad \lambda = 2am \tag{1}$$

$$\psi = m\theta = m \arctan \left(\frac{y}{x} \right) \tag{2}$$

Further considering the effect of uniform flow, if $\vec{V} = \vec{V}(x, y) = A\hat{x} + B\hat{y}$, thereby representing a uniform flow in an arbitrary direction, it can be shown that the equivalent streamline for such a flow is seen to be represented by Equation 3.

$$\psi = Ay - Bx \tag{3}$$

The combination of these 2 flows would nominally represent flow along the surface of a flat surface in an arbitrary flow. However, through initial testing, it was identified that the usage of an extended doublet, created by this series of closely placed doublets, would produce a flat profile only in extremely close proximity to the doublet sheet. Local curvature of the field lines, passing from the source to the sink of the doublet, flowing back to itself, would show local curvature that would affect the flow near the surface. Further, the given the need to represent accurate geometry, once again referencing Figure 7, concerns about modelling these exact profiles led to alternative options. The usage of a mirrored set of vortices on either side of the doublet sheet to force the streamlines to become horizontal, by means of the method of images was also considered, however, given the proximity and strength required of these vortices and their proximity to the eventual location of the fins, this idea was abandoned. Given the need to form an exact profile of desired shape, it was determined that an iterative approach of combining smaller flow elements would not be ideal. As such additional, more analytical methods were considered.

4.1   Complex Flow and Conformal Mapping

Given the need to produce an accurate and controlled flow pattern based on the expected geometry of the arrow with a desired fin, a conformal map in conjunction with complex flow was identified as the optimal solution given it's inherent flexibility. This method, in broad strokes, is capable of re-mapping a flow pattern to a desired geometry allowing analysis of flow around custom shapes. This method will be explored in the following sections.

4.2   Basic Flows Using Complex Flow

Although the velocity potential and stream function can be specified independently, as such can be nominally represented by $\phi(x, y)$ and $\psi(x, y)$, an additional formulation through the use of complex numbers can be considered. Consider the function $f(z)$ where $z \in \mathcal{C}$. If z is given to be a complex number of the from $x + jy$ then it can be shown that the velocity potential function and stream function can both be additionally be represented as functions of z, $\phi(z)$ and $\psi(z)$, respectively. Given this formulation, it can be shown that a function $f(z) = \phi(z) + j\psi(z)$, where the velocity potential and stream function exists as the real and imaginary components, respectively, additionally satisfies the Laplace equation as required of potential flow [9, Chapter 8].

Starting with uniform flow, a rederivation requires the use of both the velocity potential and the stream function, which is illustrated in the following process.

$$A = u = \frac{\partial \phi}{\partial x} = \frac{\partial \psi}{\partial y} \implies \phi = Ax + f(y), \quad \psi = Ay + f(x)$$

$$B = u = \frac{\partial \phi}{\partial y} = -\frac{\partial \psi}{\partial x} \implies \phi = By + f(x), \quad \psi = -Bx + f(y)$$

$$\implies \phi = Ax + By, \quad \psi = -Bx + Ay$$

$$\implies f(z) = \phi + j\psi = Ax + By + j(-Bx + Ay) = Ax - jBx + jAy + By$$

Noting that the function $U_\infty z \exp(-j\alpha)$ expands into $Ax - jBx + jAy + By$, it can be therefore stated that uniform flow, at an arbitrary angle as given by the "angle of attack" α, is given below Equation 4 [pg. 560] [9].

$$f(z) = U\infty z \exp(-j\alpha) \tag{4}$$

Using the definition of the velocity potential function of doublet flow, as given below in Equation 5 [pg. 550] [9], utilization with the previously defined stream function for this flow can be used to identify the complex equivalent.

$$\phi = \frac{\lambda x}{x^2 + y^2} \tag{5}$$

This process to convert the doublet to its complex form is described below.

$$f(z) = \phi + j\psi$$

$$= \frac{\lambda x}{x^2 + y^2} - j\frac{y}{x^2 + y^2}$$

$$= \frac{\lambda(x - jy)}{x^2 + y^2}$$

$$= \frac{\lambda z^*}{zz^*}$$

$$= \frac{\lambda}{z}$$

As such, for future usage, the complex form of a doublet is provided as the form described in Equation 6.

$$f(z) = \frac{\lambda}{z} \tag{6}$$

A similar process can be used with a vortex to yield the relation as presented below in Equation 7 [9, pg.560]. It should be noted that z_0 is an offset used to shift the center of the vortex to a different spatial location.

$$f(z) = -jK \ln(z - z_0) \tag{7}$$

In the same manner in which non-complex flow solutions can be added while still satisfying the Laplace equation governing potential flow, the same argument can be made for a linear combinations of complex solutions. As such, a circulating cylinder can additionally be represented below in Equation 8.

$$f(z) = U_\infty z \exp(-j\alpha) + \frac{\lambda}{z} - jK \ln(z) \tag{8}$$

As recommended by [9, pg.552], the use of doublet strength $\lambda = U_\infty a^2$, where a is the radius of a desired circle with streamline value of 0, should be used to allow a simplistic method of analyzing the flow. This relation, in addition to the prescribed doublet strength, with radius of 1, is presented below in Figure 8 presented a xy-plane which is input into $f(z)$ using the corresponding complex equivalent z. The graph on the left-hand side of this figure is the velocity potential, which is taken to be the real values of the function while the streamlines on the right are plotted from the imaginary components of the field.
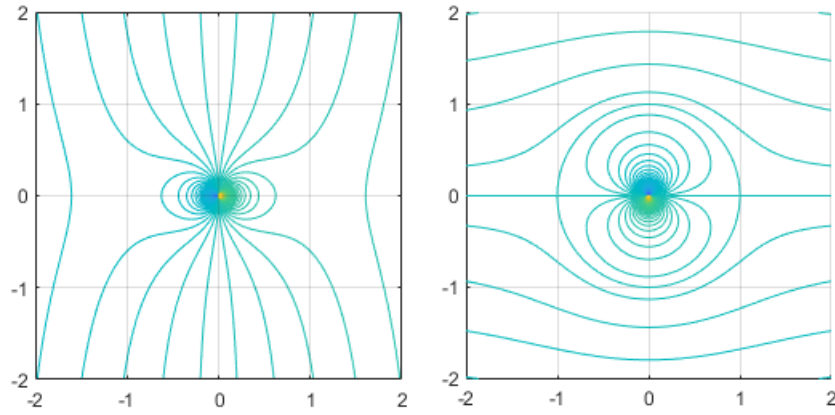

Figure 8: Complex Circulating Cyclinder for Velocity Potential and Streamlines

It was later identified through testing that the factor $\exp(j\alpha)$ would need to be introduced to the doublet term, given by λ/z in order to maintain the circular profile in the streamline if the uniform flow was to be angled. This modified form of this expression is given below by Equation 9.

$$f(z) = U_\infty z \exp(-j\alpha) + \frac{\lambda}{z} \exp(j\alpha) - jK \ln(z) \tag{9}$$

Although the streamlines can be plotted, further operations can easily be performed on this complex plane. For further use, the variable w will be used to represent the output of $f(z)$, in other words $w = f(z)$.

4.3   Velocity and Pressure from Complex Flow

To identify the velocities of the flow within the region contained by w, the derivative of w with respect to z must be first determined. Similar to derivatives of real derivatives, numerical derivatives between these two complex planes can additionally be computed. However, subject to the laws of complex analysis, a derivative in the complex plane will converge to the same value irrespective of the direction in which the derivative was taken [10]. This has enormous benefits on model development given that a numerical derivative can

9

be taken between z and w. Given the real and imaginary components of this derivative, the components of velocity can be readily identified from Equation 10 [9, pg. 559].

$$\frac{dw}{dz} = \frac{df}{dz} = u - jv \tag{10}$$

More practical forms of the preceding equation are captured below in Equation 11.

$$u = \mathrm{Re}\left(\frac{dw}{dz}\right), \quad v = -\mathcal{I}\Updownarrow \frac{dw}{dz} \tag{11}$$

This derivative, in addition to deriving the flow field, allows placing of the streamline position. Although a conformal mapping, as described in the following section, will be used to remap the flow around the arrow profile, the trailing stagnation point must be moved to the trailing stagnation point. This can be achieved by setting the velocity to 0 at a stagnation point on the disk, thus having distance R, thereby being at position $z = R\exp(j\theta)$.

$$\begin{aligned}
\frac{df}{dz} &= \frac{d}{dz}\left(f(z) = U_\infty z\exp(-j\alpha) + \frac{\lambda}{z}\exp(j\alpha) - jK\ln(z)\right) \\
&= -\frac{jK}{z} + U_\infty\exp(-j\alpha) - \frac{\lambda\exp(j\alpha)}{z^2} \\
&= -\frac{jK}{z} + U_\infty\exp(-j\alpha) - \frac{R^2 U_\infty\exp(j\alpha)}{z^2}
\end{aligned}$$

Substitution of this stagnation point and the previously specified doublet strength leads to the following.

$$\begin{aligned}
\left.\frac{df}{dz}\right|_{z=R\exp(j\theta)} &= U\infty\exp(-j\alpha) - U\infty\exp(j\alpha)\exp(-j2\theta) - \frac{jK}{R}\exp(-j\theta) \\
&= u - jv = 0
\end{aligned}$$

Further re-arranging the preceding relation and solving for the vortex strength allows finding the vortex strength necessary to enforce the Kutta condition thereby producing the correct vortex effect across the arrow when the uniform flow angle is changed. Given that it is assumed that the fin obeys the requirement to keep the stagnation point at the tail in all types of flows, given the similarity to airfoils [9, Chapter 8], and that the conformal mapping in the next session preserves the angles of the leftmost and rightmost points for arrow profiles mirrored across the x-axis, nominally the position of this stagnation point should be located at $(1,0)$ and thus for all cases analyzed in this report, $\theta = 0$.

$$K = -2RU_\infty\sin(\alpha - \theta) \tag{12}$$

Given that the velocity of the flow field is known, with the magnitude of the velocity readily calculated as $V = \sqrt{u^2 + v^2}$, the pressure can be computed readily using the Bernoulli equation given that potential flow already implies the existence of streamlines. As such, the pressure distribution can be calculated using Equation 13, assuming that the effect of gravity is negligible given the small size of the arrow. It should be noted that V_0 and p_0 refer to the free stream velocity and pressure.

$$p = \frac{1}{2}\left(V_0^2 - V^2\right) + p_0 \tag{13}$$

4.4 Variable Conformal Mapping

As highlighted previously, the existence of specific fin geometry that differs from the nominal superposition of basic flow patterns requires the use of a more advanced numerical technique. Starting from the original z field, the flow variables, specified as w are computed. An additional function, known as a conformal map, changes the domain of w to a new plane as . Primarily, the conformal map simply acts to change the positions of the input while keeping the same flow pattern. As such, streamlines and velocity potential lines will be moved but their connections will be preserved. A common example of a conformal transformation is given to be the Joukowski tranformation in airfoil analysis [9, Chapter 8].

The geometry of each arrow, including the desired fin profiles, were first generated using a combination of various primitive functions. An example of such an arrow geometry can be found below in Figure 9.
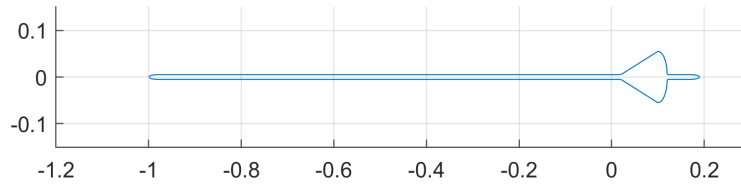
Figure 9: Example Arrow Geometry

To ensure the most stability in the resulting Fourier transformation, the spacing of the points as specified in the geometry was first made uniform to ensure that any generated mapping would not favor one side of the geometry. These points were then expressed as points within the plane, thereby becoming complex positions wherein their x- and y-positions represented the real and imaginary components, respectively. The ratio of these geometry positions over that of a unit sphere were then taken. This effectively describes the conformal mapping for only the points on the unit circle in the z plane itself. As such, an additional method would be required to generalize this function to the local area.

Given the complex positions belonging to the unit circle, a Taylor series fit, as seen below in Equation 14 with coefficients calculated through least-squares, was considered to generate the ratio as a function of the input position (in the z plane).

$$f(z) = \sum_{i=0}^{N} k_i z^i \tag{14}$$

Based on both the required magnitude and phase angle, given this ratio is also complex, the Taylor series was unable to show increasing convergence of a test profile even at the higher order of 20. These results can be seen below in Figure 10.
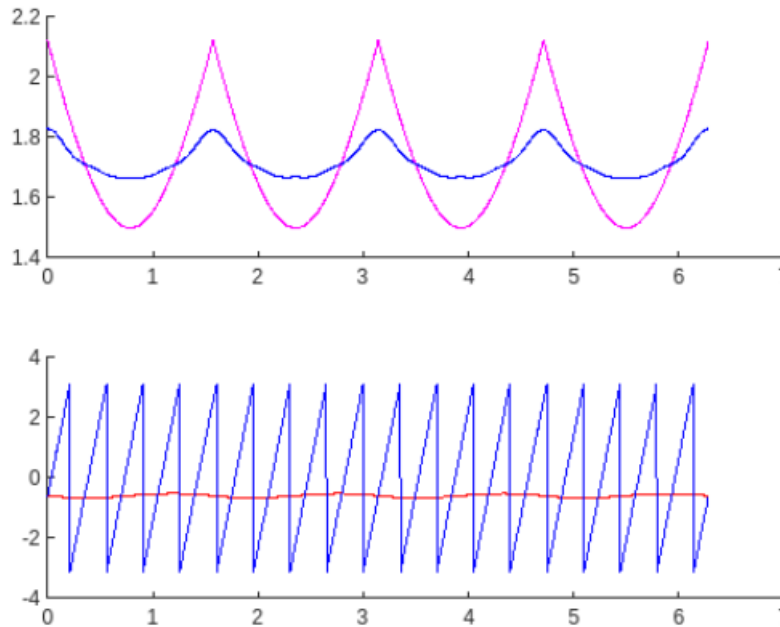
Figure 10: Poor Taylor Convergence of Conformal Fit

Given the poor convergence of the Taylor series, a Fourier series was considered instead. The coefficients of the Fourier series can be calculated below using Equation 15 [10] while the actual Fourier series itself is presented below in Equation 16 [10]. It should be noted that through experimentation it was determined that the Fourier series was only convergent to a complex value when a real value was provided as an input. As such, only the angle of the disk was able to be used as an input.

$$c_n = \frac{1}{2L} \int_{-L}^{L} f(x) \exp\left(-\frac{jn\pi x}{L}\right) \tag{15}$$

$$f(x) = \sum_{n=-\infty}^{\infty} c_n \exp\left(\frac{jn\pi x}{L}\right) \tag{16}$$

For the same test profile as used with the Taylor series, it was seen that rapid and good convergence was readily able to be achieved with a Fourier series as presented below in Figure 11.
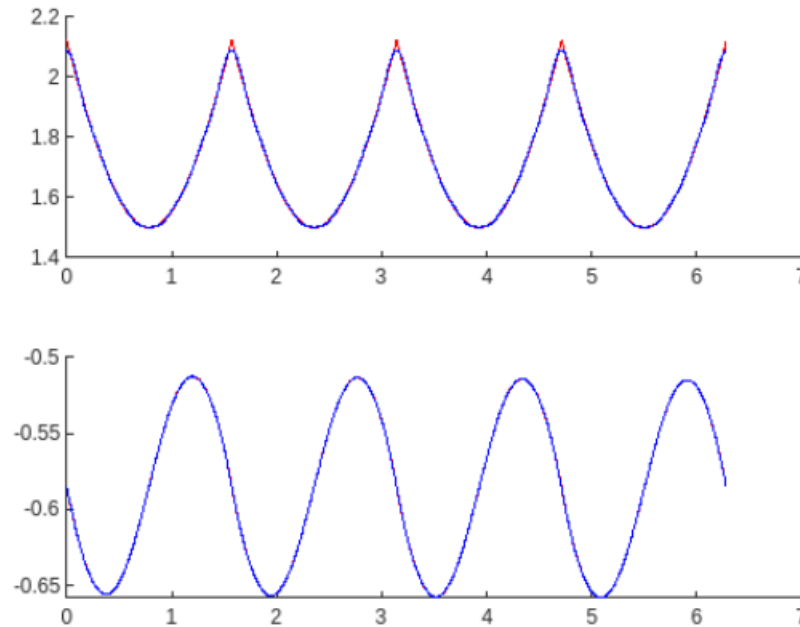
Figure 11: Rapid Fourier Convergence of Conformal Fit

Given the good convergence of the Fourier series, it was chosen for future use. Based on the example profile as seen above in Figure 9, the use of a Fourier transform in approximating the conformal mapping is given below in Figure 12.
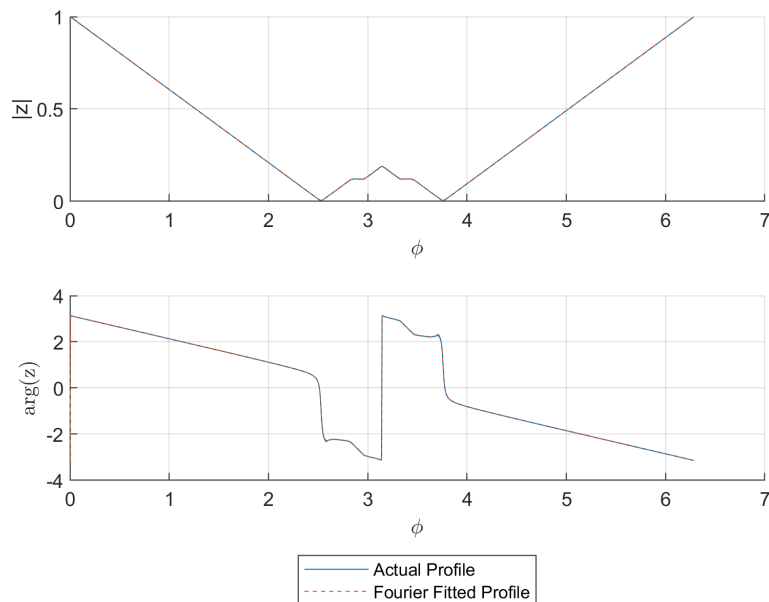
Figure 12: Fit of Fourier Series to Example Arrow Geometry Conformal Map for Disk

Although this profile matches very well for the transformation of the disk, with radius 1 given only the angle could be chosen, to the expected geometry, from the z to planes, respectively, this function is not sufficient on

its own to constitute a full conformal mapping. As such an additional modification to the Fourier series would be needed. In [11], it is suggested that the Fourier series be modified such that a radial term is introduced into each term of the series.

As such, this modified conformal map, as seen below in Equation 17 was used for throughout the remainder of this paper.

$$f(\theta, r) = \sum_{n=-\infty}^{\infty} c_n r^{abs(n)} \exp\left(\frac{jn\pi\theta}{L}\right) \tag{17}$$

It should be noted that the given profiles examined in detail in the remainder of paper, the Fourier coefficients associated with each profile can be found in the Appendices.

4.5   Arrow Velocity and Pressure Distributions

Similarly to the velocity and pressure distributions as calculated for the circulating sphere, the velocity distribution and pressure distribution must once again be calculated given that the domain of the flow has changed from the coordinates as specified in z to ζ. As opposed to calculating df/dz, as originally calculated, df/d must instead. With the example air foil as previously described from Figure 9, calculation of the velocity magnitude, from application of Equation 11 and the pressure, from application of Equation 13, can be seen below in Figure 13 and Figure 14, respectively.
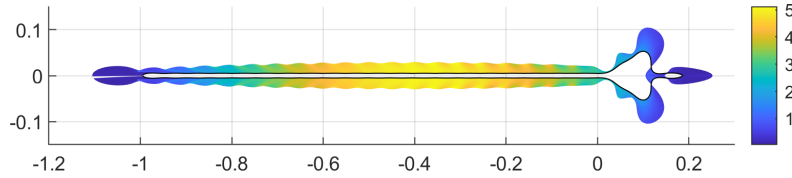
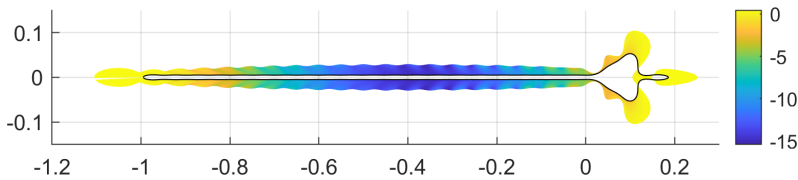Figure 13: Velocity Magnitude Profile Around Example Arrow

Figure 14: Pressure Magnitude Profile Around Example Arrow

Additional considerations were however made with respect to the behaviour of the pressure in what is assumed to be the wake. Given that it was assumed that the flow separates at a sharp adverse pressure gradient, it is assumed that the flow separates from the surface of the arrow at *the closest local pressure minimum along the surface to each peak*. In comparison with Figure 15, which was computed from a representative fluid flow model, it can be seen that this is a correct assumption.

The figure belows will show sht eflow conditions about the prototypical fin and trail computed from CFD
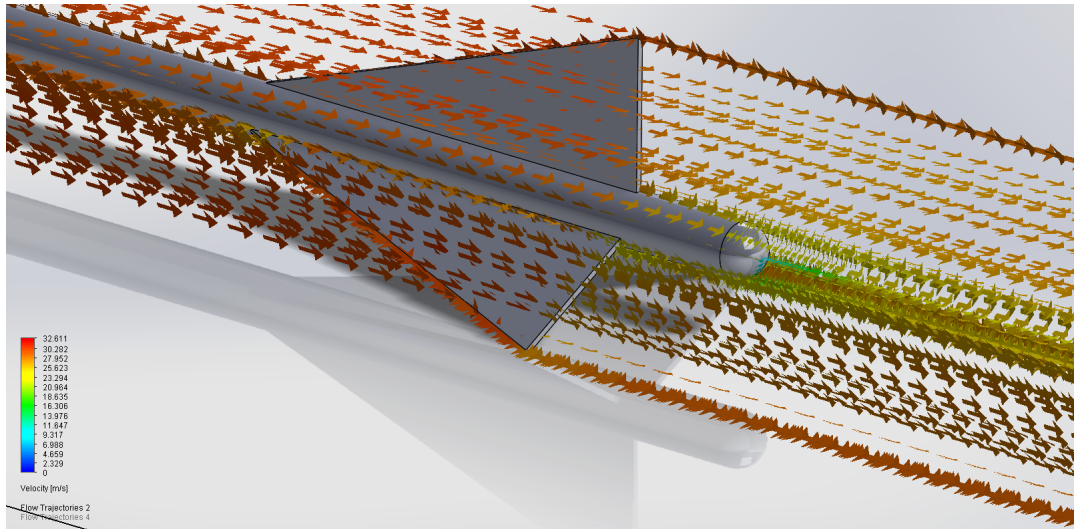
Figure 15: Flow Conditions About Prototypical Fin and Tail Computed from CFD

Given that a vacuum pressure drag is expected in this "wake", attempts were made to identify a suitable model to simulate the pressure. However, common engineering models and approximations, including the Jensen model are designed for rotors and turbines and require the use of dimensionless parameters associated with power in their calculations [**?**]L. As such, it was necessary to develop an approximate model for the boundary layer flow. Given the intention is to generate a vacuum pressure, on the back surface of the fin, between these "separation" points, the pressure was adjusted such that the new pressure was equal to a pressure interpolated between the pressures of the separation points minus the pressure expected from the potential flow model. The goal of this region is to create a pressure deficit to induce some level of suction and pressure drag from the wake.

The pressure force was computed through the use of a surface integral of the modified wake pressure distribution about the surface of the body. The differential pressure force was calculated at the center of each line "segment" connecting local vertices in the profile. For the example arrow, used in this section, the differential pressure forces are shown in Figure 16. It should be noted that the total pressure drag is given by the vector summation.
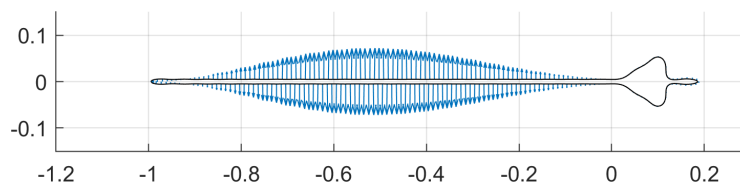

Figure 16: Differential Pressures About Example Arrow Profile

4.6   Skin Friction Modelling

For modelling of the skin friction on the surface of the arrow, it was first necessary to identify the forward leading stagnation point. This point was identified simply as the maximum pressure point towards the leading edge of the arrow with respect to the external flow. Given that it is known that the viscous forces are approximately 0 in the wake [9], the surfaces for which the skin friction contributes force were identified to

start from the forward stagnation point and terminate at the top and bottom "separation" points, as previously identified.

4.6.1 Laminar Region

Using the laminar velocity profile, seen blow in Equation 18, as proposed by Prandtl [6, pg. 455], the wall skin friction, displacement, and momentum thicknesses were computed using the standard formulae as seen below in Equation 19, 20, and 21.

$$\frac{u}{U_e} = \left(\frac{2y}{\delta} - \frac{y^2}{\delta^2} \right) \tag{18}$$

$$\delta^* = \int_0^\delta \left(1 - \frac{u}{U_e} \right) dy = \frac{\delta}{3} \tag{19}$$

$$\theta = \int_0^\delta \frac{u}{U_e} \left(1 - \frac{u}{U_e} \right) dy = \frac{2\delta}{15} \tag{20}$$

$$\tau_w = \mu \frac{\partial u}{\partial y} \bigg|_{y=0} = \frac{2U_e\mu}{\delta} \tag{21}$$

These equations were substituted into the Momentum-Integral Equation (MIE) and the rate of growth of the laminar boundary layer was able to be found and is presented below in Equation 22.

$$
\begin{aligned}
\frac{\tau}{\rho} &= \frac{d}{dx}\left(U_e^2\theta\right) + \delta^* U_e \frac{dU_e}{dx} \\
&= \frac{d}{dx}\left(U_e^2 \frac{2\delta}{15}\right) + \frac{\delta}{3} U_e \frac{dU_e}{dx} \\
&= \frac{2}{15}U_e^2 \frac{d\delta}{dx} + \frac{2}{15}2U_e \frac{dU_e}{dx}\delta + \frac{\delta}{3}U_e \frac{dU_e}{dx} \\
\frac{2U_e\mu}{\delta\rho} &= \frac{2}{15}U_e^2 \frac{d\delta}{dx} + \frac{3}{5}\delta U_e \frac{dU_e}{dx}
\end{aligned}
$$

$$\frac{d\delta}{dx} = \frac{15\nu}{\delta U_e} - \frac{9}{2}\frac{\delta}{U_e}\frac{dU_e}{dx} \tag{22}$$

While the local Reynolds number is under the critical Reynolds number of 5×10^5, the laminar boundary layer growth was computed and the wall skin frictional forces were calculated using Equation 21 and the discretized surface in the same manner as the calculation of the pressure forces.

4.6.2 Turbulent Region

In this region, Prandt's 7th law velocity approximation, seen in Equation 23 was necessary to compute the turbulent skin friction drag. However, given that the wall skin friction with this approximate relation is discontinuous at the wall, it was necessary to employ the growth of the turbulent boundary layer on a flat plate, seen in Equation 24 given that the previous method of calculating boundary layer growth is not possible.

$$\frac{u}{U_0} = \left(\frac{y}{\delta}\right)^{1/7} \tag{23}$$

$$\frac{\overline{\delta}}{x} = \frac{0.16}{\mathrm{Re}_x^{1/7}} \tag{24}$$

As before the displacement and momentum thicknesses can be computed as seen below in Equation 25 and 26, respectively.

$$\theta = \frac{7}{72}\delta \tag{25}$$

$$\delta^* = \frac{\delta}{8} \tag{26}$$

Using the MIE equation again but with the turbulent profile, the skin friction, seen in Equation 27, and shear force was able to be calculated at each different element of the surface.

$$\begin{aligned}
\frac{\tau}{\rho} &= \frac{d}{dx}\left(U_e^2\theta\right) + \delta^* U_e \frac{dU_e}{dx} \\
&= \frac{7}{72}\frac{d}{dx}\left(U_e^2\delta\right) + \frac{\delta}{8}U_e\frac{dU_e}{dx} \\
&= \frac{7}{72}2U_e\frac{dU_d}{dx}\delta + \frac{7}{72}U_e^2 * \frac{d\delta}{dx} + \frac{\delta}{8}U_e\frac{dU_e}{dx}
\end{aligned}$$

$$\implies \tau = \rho\left[\frac{23}{72}U_e\delta\frac{dU_e}{dx} + \frac{7}{72}U_e^2\frac{\delta}{dx}\right] \tag{27}$$

For the example arrow, the computed skin friction forces are shown below in Figure 17.
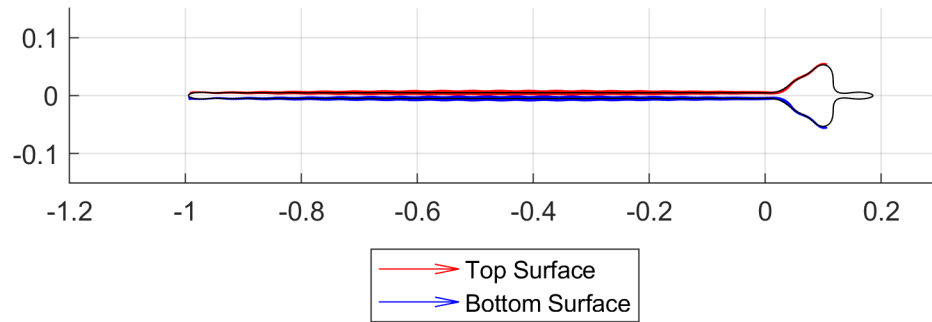
Figure 17: Skin Friction Drag for the Example Arrow

4.7 Stability and Coefficient Calculations

The coefficients of drag, lift, and moment (measured from the tip) on the arrow were computed with Equations 28, 29, and 30 [**?**], respectively. The static margin was simply defined as the distance towards the aft of the arrow from the overall center of pressure (from the pressure forces and not skin friction). It should be noted that the span (b) for this analysis is assumed to be unit length of 1.

$$c_d = \frac{D}{0.5\rho b L_c U_\infty^2} \tag{28}$$

$$c_L = \frac{L}{0.5\rho b L_c U_\infty^2} \tag{29}$$

$$c_m = \frac{M}{0.5\rho U_\infty^2 b L_c^2} \tag{30}$$

5   Results

5.1   Old English KL

In this section, the results of the simulation for the Old English KL fin will be analyzed.
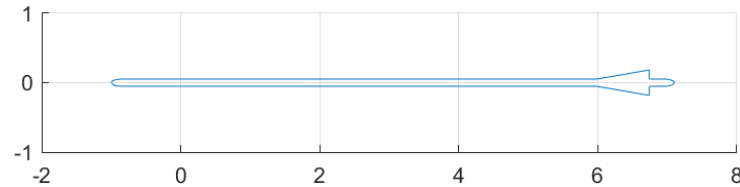
Figure 18: Old English KL Arrow Profile

The following figure will show the streamline around the flow computed from previous discussed method,
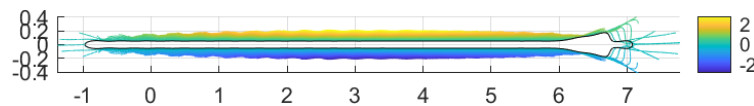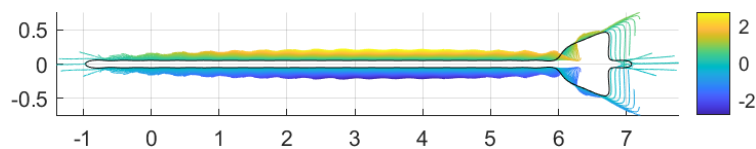

Figure 19: Streamline around Arrow Surface

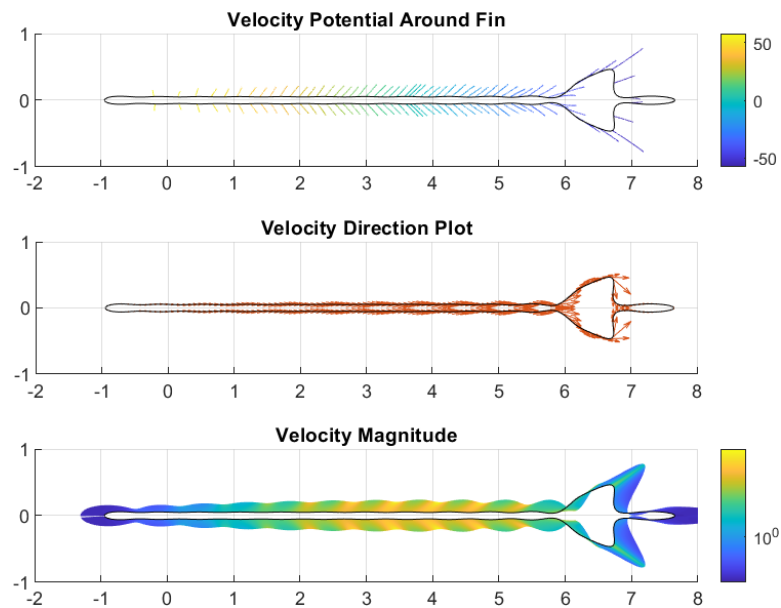The velocity profile of the flow around arrow is show as following,
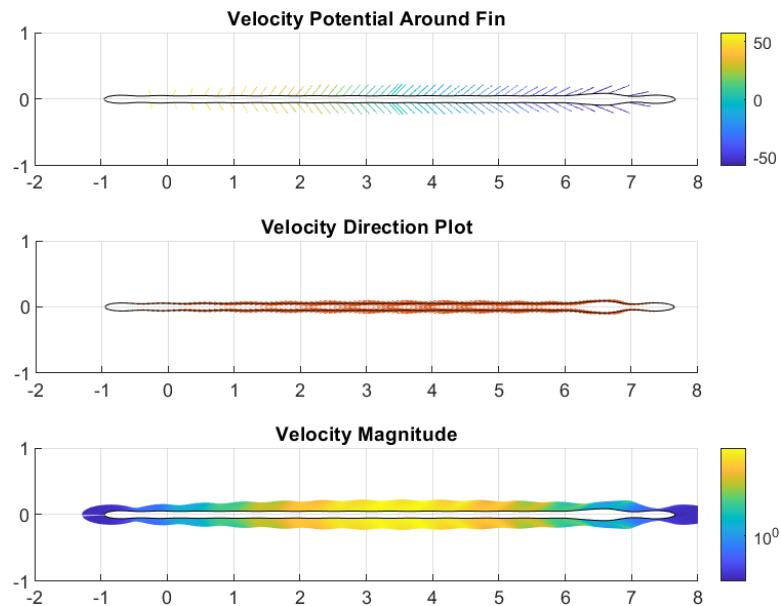
Figure 20: Velocity Profile of Flow around Arrow Surface

The pressure including tangential and normal distribution of the flow around the arrow is shown as following,
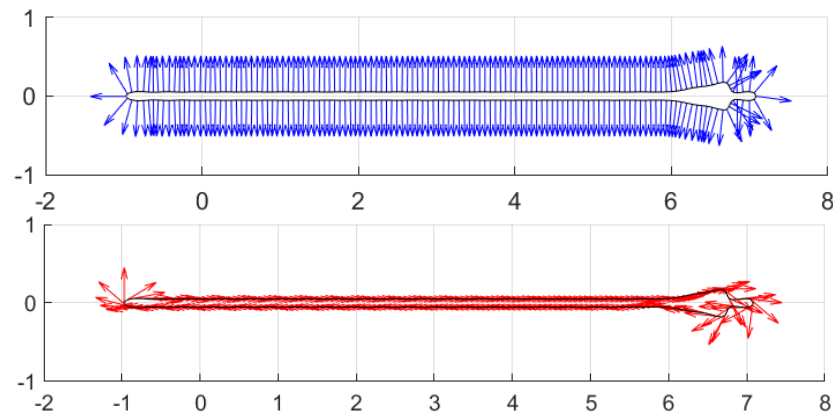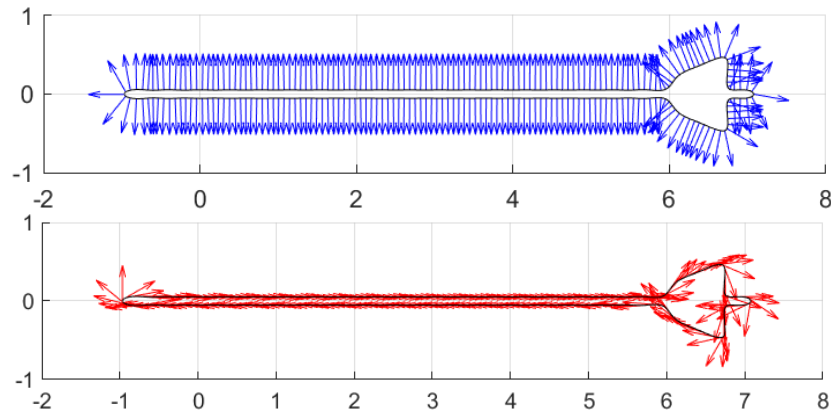
Figure 21: Old English KL Surface Normal and Surface Tangent Plots

The total pressure distribution around the arrow is shown as following:
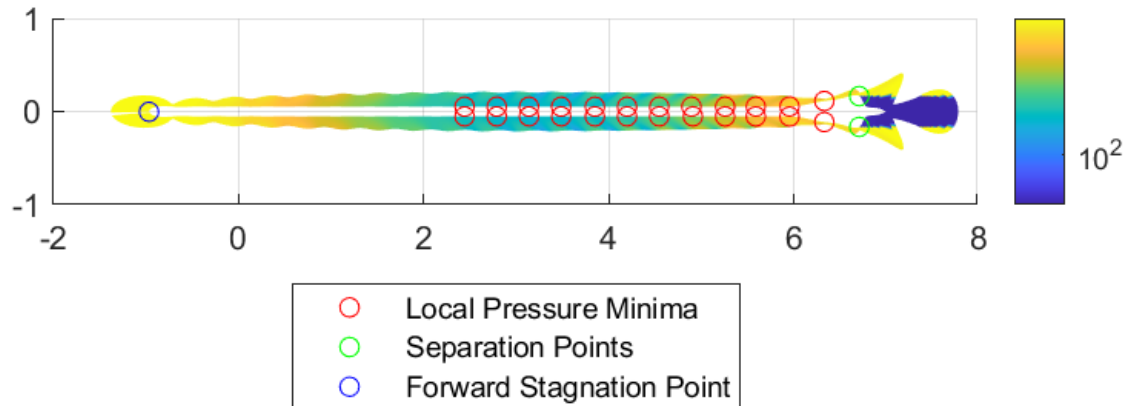
Figure 22: Total Pressure Distribution of Arrow with Wake Region Simulated

The skin drag friction drag on surface of arrow is simulated as following figure,
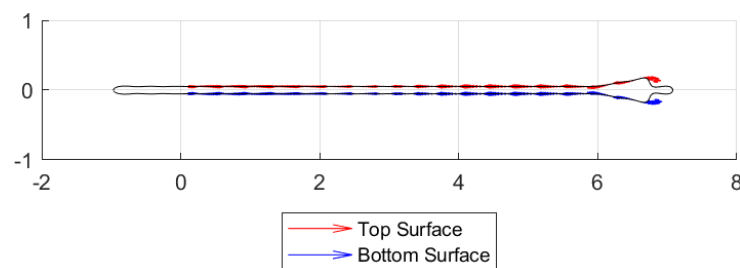
Figure 23: Skin Drag Coefficient on Surface Profile

From the concept of the boundary layer, as velocity increases, the

5.2   Old English SL

In this section, the results of the simulation for the Old English SL fin will be analyzed.
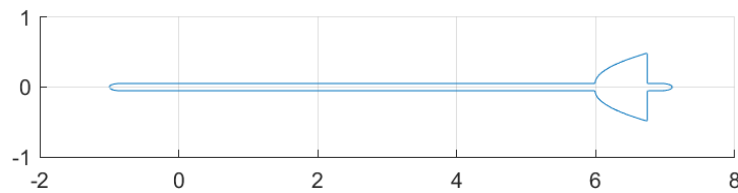
Figure 24: Old English SL Arrow Profile

The following figure will show the streamline around the flow computed from previous discussed method,

Figure 25: Streamline around Arrow Surface

The velocity profile of the flow around arrow is show as following,

Figure 26: Velocity Profile of Flow around Arrow Surface

The pressure including tangential and normal distribution of the flow around the arrow is shown as following,

Figure 27: Old English SL Surface Normal and Surface Tangent Plots

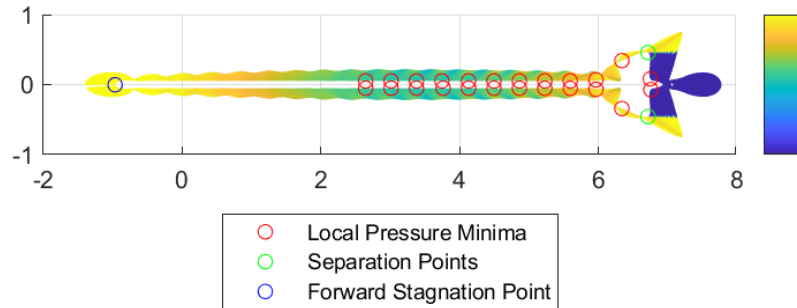The total pressure distribution around the arrow is shown as following:

Figure 28: Total Pressure Distribution of Arrow with Wake Region Simulated

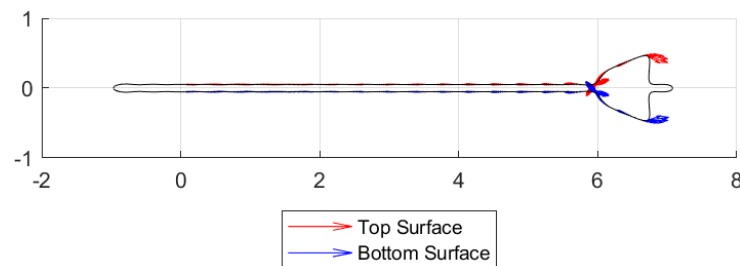The skin drag friction drag on surface of arrow is simulated as following figure,

Figure 29: Skin Drag Coefficient on Surface Profile

5.3   Pope and Young

In this section, the results of the simulation for the Pope and Young fin will be analyzed.
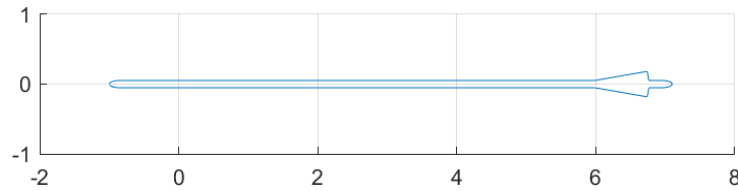
Figure 30: Pope and Young Arrow Profile

The following figure will show the streamline around the flow computed from previous discussed method,
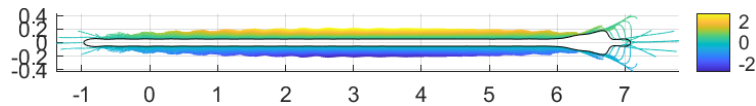

Figure 31: Streamline around Arrow Surface

The velocity profile of the flow around arrow is show as following,
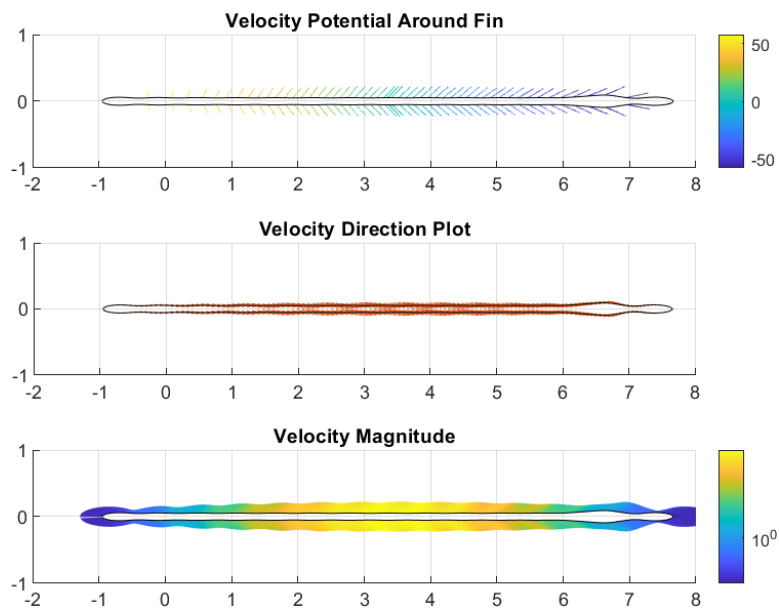

Figure 32: Velocity Profile of Flow around Arrow Surface

The pressure including tangential and normal distribution of the flow around the arrow is shown as following,
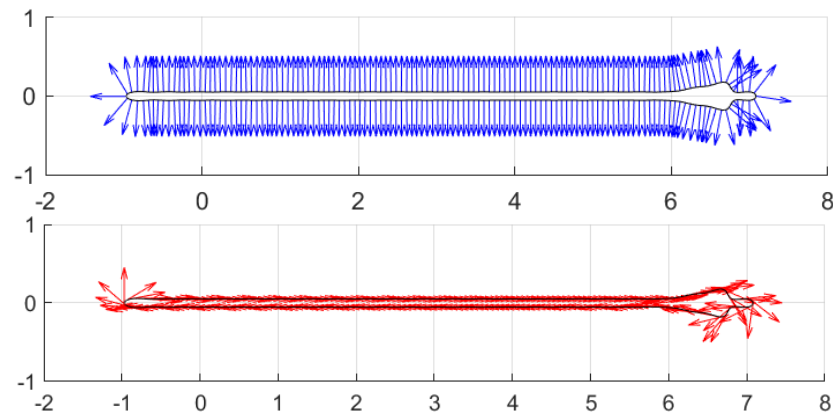
Figure 33: Pope and Young Surface Normal and Surface Tangent Plots

The total pressure distribution around the arrow is shown as following:
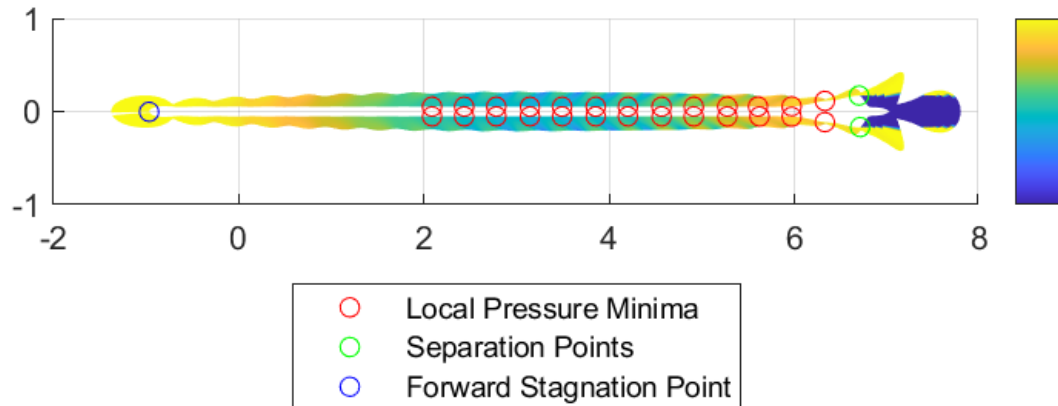

Figure 34: Total Pressure Distribution of Arrow with Wake Region Simulated

The skin drag friction drag on surface of arrow is simulated as following figure,

Figure 35: Skin Drag Coefficient on Surface Profile

5.4   Shield

In this section, the results of the simulation for the Shield fin will be analyzed.
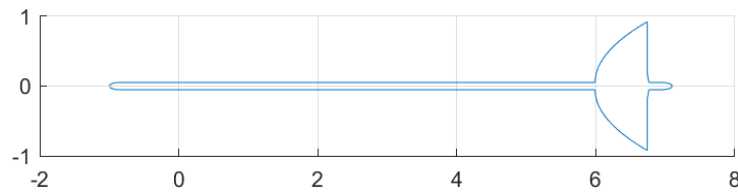
Figure 36: Shield Arrow Profile

The following figure will show the streamline around the flow computed from previous discussed method,

Figure 37: Streamline around Arrow Surface

The velocity profile of the flow around arrow is show as following,

Figure 38: Velocity Profile of Flow around Arrow Surface

The pressure including tangential and normal distribution of the flow around the arrow is shown as following,

Figure 39: Shield Surface Normal and Surface Tangent Plots

The total pressure distribution around the arrow is shown as following:

Figure 40: Total Pressure Distribution of Arrow with Wake Region Simulated

The skin drag friction drag on surface of arrow is simulated as following figure,
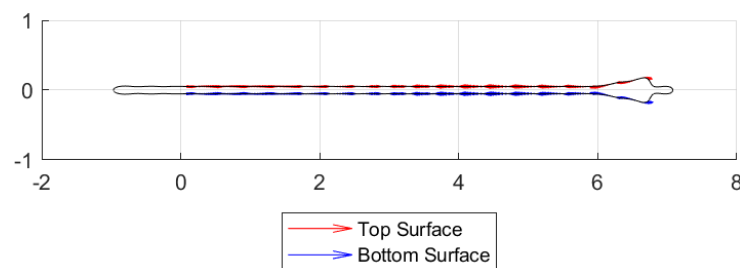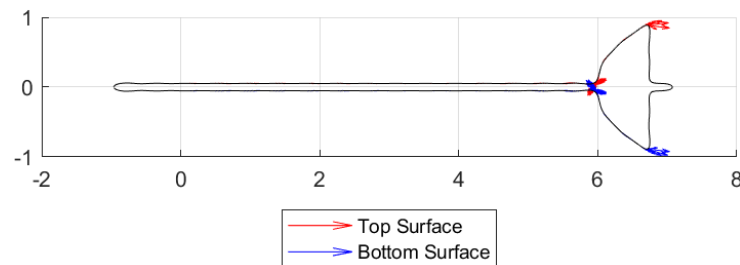

Figure 41: Skin Drag Coefficient on Surface Profile

5.5   French Curve

In this section, the results of the simulation for the French Curve fin will be analyzed.
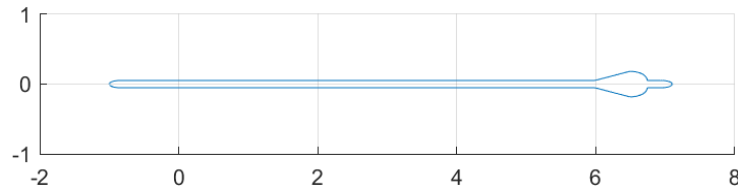
Figure 42: French Curve Arrow Profile

The following figure will show the streamline around the flow computed from previous discussed method,
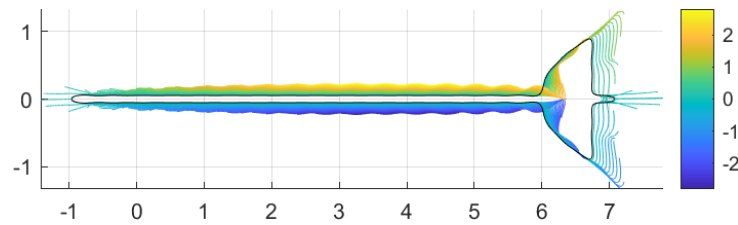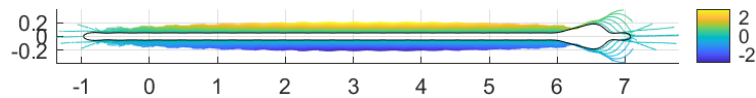

Figure 43: Streamline around Arrow Surface

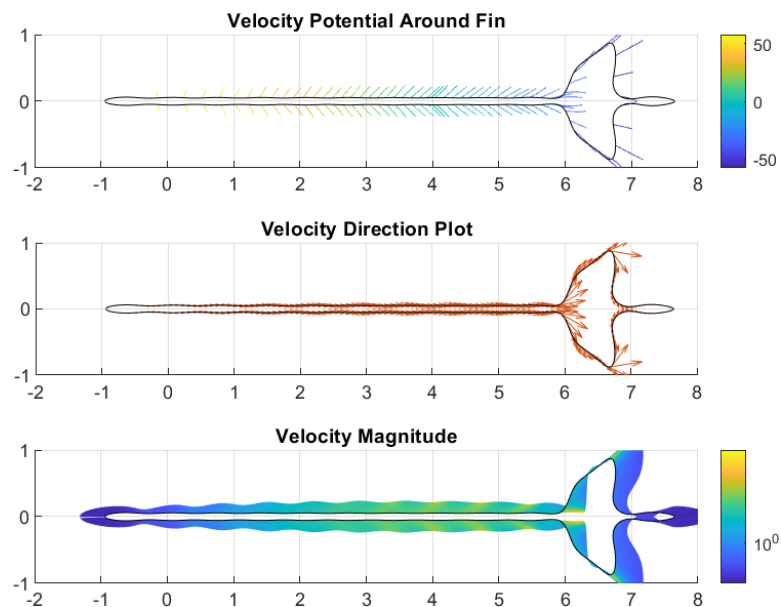The velocity profile of the flow around arrow is show as following,
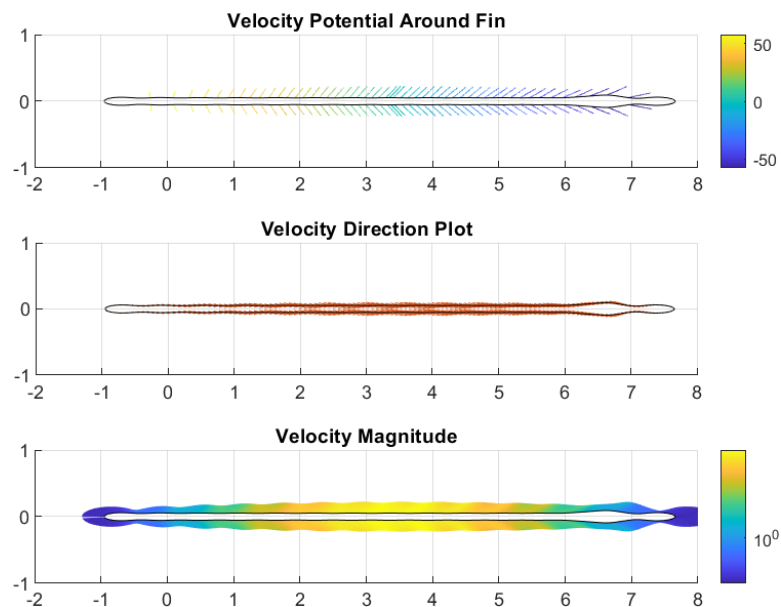
Figure 44: Velocity Profile of Flow around Arrow Surface

The pressure including tangential and normal distribution of the flow around the arrow is shown as following,
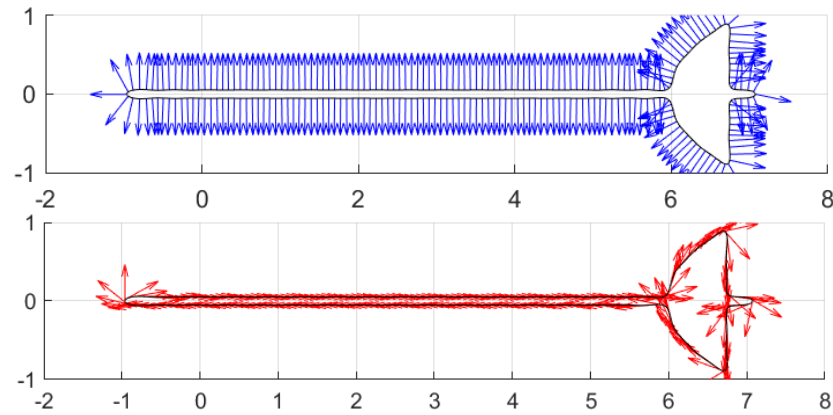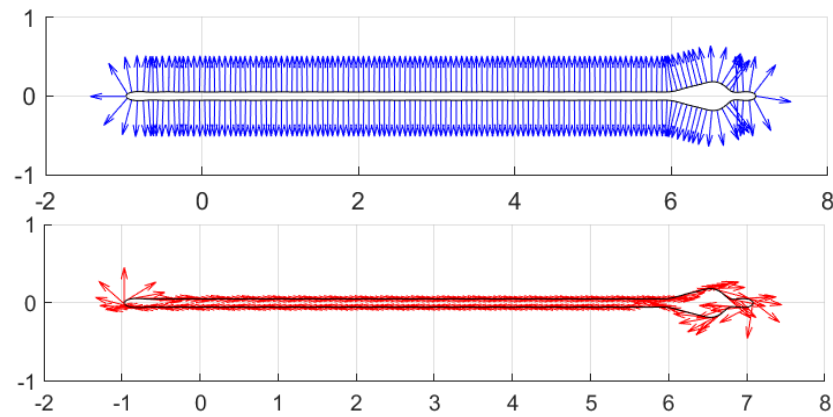
Figure 45: French Curve Surface Normal and Surface Tangent Plots

The total pressure distribution around the arrow is shown as following:
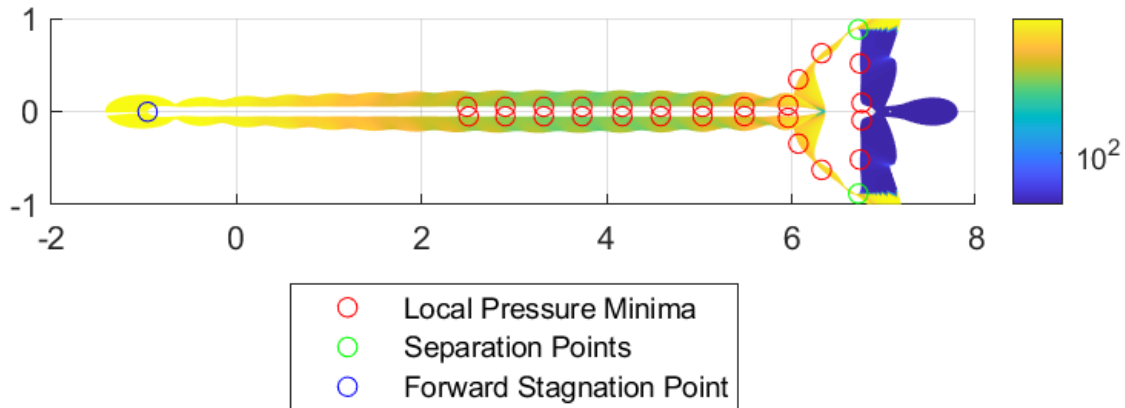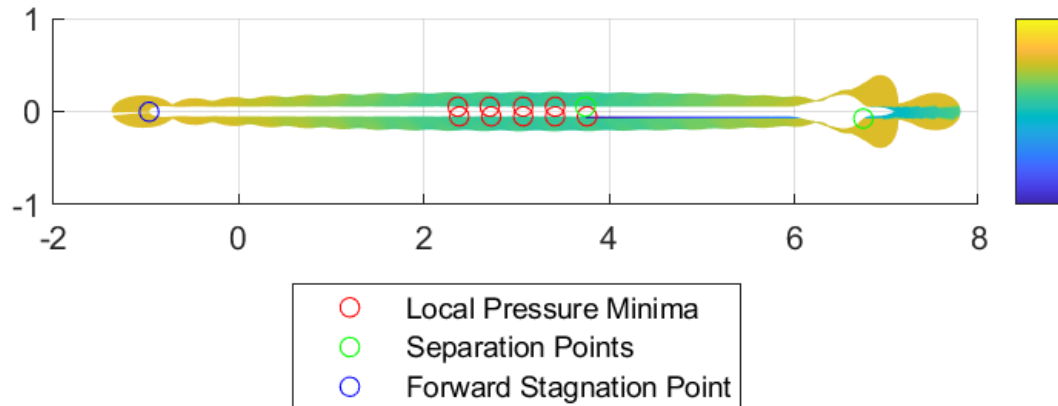

Figure 46: Total Pressure Distribution of Arrow with Wake Region Simulated

The skin drag friction on the surface of the arrow is simulated as following figure,
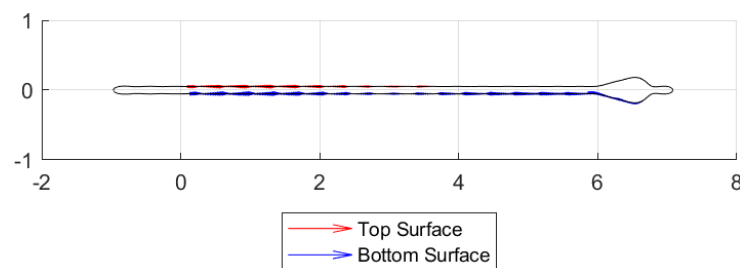
Figure 47: Skin Drag Coefficient on Surface Profile

6   Analysis

The following section will further discuss about the flow behavior approaching the tips, fins, and the tail of the arrow.

From the simulation, the following properties were calculated for each fin type.

	Old English KL	Old English SL	French Curve	Shield	Pope and Young
Arrow Tip Moment (N$\times M$)	-8.36 $\times 10^3$	-7.80 $\times 10^3$	1.49 $\times 10^4$	-6.28 $\times 10^3$	-2.35 $\times 10^6$
Drag (N)	4.71 $\times 10^4$	1.63 $\times 10^5$	4.88 $\times 10^4$	3.48 $\times 10^5$	-1.07 $\times 10^4$
Drag Coefficient	10.84	37.52	11.24	80.27	-2.45
Lift (N)	-1.16 $\times 10^3$	-1.02 $\times 10^3$	1.91 $\times 10^3$	-832.49	-3.83 $\times 10^5$
Lift Coefficient	-0.27	-0.23	0.44	-0.19	-88.35
Moment Coefficient	-0.24	-0.22	0.43	-0.18	-67.15
Static Margin	0.40	0.45	0.49	0.53	0.26

Table 1: Flow Properties for Different Fin Types

6.1   Similar Behaviors of Flow around the Arrow

6.1.1   Pressure and Velocity Profile Analysis

From the pressure profiles given in the Results Section, it can be seen that a stagnation point occurs right at the tip of the arrow head. With the assumption that there is no effect on the weight of the arrow, the flow stagnating at this point resulted in the pressure decreases as it travels around the tip of the arrow, which is noted as *favorable pressure gradient* [6, pg. 452]. Once it travels past the tip and moves along the main body of the arrow, the normal pressure and tangent pressure of the fluid converges and stabilizes before encountering the fin. This can be explained using the flat plate method assumption on the main body of the arrow, which results in no pressure gradient along the main body direction. Similar behavior of pressure distribution on the fin is observed as well due to the assumption of flat plate. However, once the the fluid passes the fin, the pressure distribution is observed to be more chaotic depending on the type of the arrow

fin. It can be observed that the boundary layer encounters increasing pressure and the boundary layer start to separate, resulting in a wake region at the tail. This phenomenon is called *adverse pressure gradient* according [6, pg. 452]. Once it passes the fin of the arrow, the flow generally become more stable, however, the pressure decrease significantly, resulting in a vacuuming at the end of the arrow. It can be explained that after layer separation following the fin, the flow becomes stable along the straight sector of the remaining body of the arrow before it encounters the end cap of the arrow. This will cause a decrease in the pressure resulting in a minimal wake region at the tail unlike region after the fin.

For velocity profiles, as the uniform flow approaches the tip of the arrow, assuming that the angle of attack is 0 degrees, the stagnation point is at the tip of the arrow, and the velocity is 0. Using the Old English KL fin type as an example, the stagnation point can be seen from the magnitude of the velocity plot below.
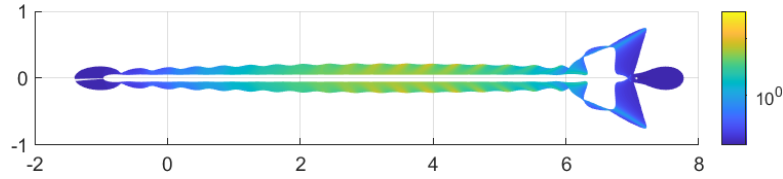

Figure 48: Velocity Magnitude Distribution along the Arrow Surface - Old English KL

The velocity at the tip starts at a magnitude of $0\,\text{m/s}$. As it travels around the tip, it should be noted that the velocity magnitude increases and once it passes the tip of the arrow, the velocity of the flow increases due to minimal resistance along the surface of the arrow. However, as it approaches the fin of the arrow, it once again decreases the velocity due to interference of the fin feature which results in a slight decrease in velocity once the fluid passes the tail. It can be reasoned that the model is simulated based on the Bernoulli Principles, therefore, as the pressure at the rear increases, the velocity will decrease at the rear location.

Similar to the results seen when analyzing the pressure plots, when looking at the velocity profiles for each fin profile, it can be seen that the velocity decreases by a large amount at the stagnation point at the arrow tip as a result of the build up of fluid. The high pressure from the build up of fluid drives the fluid at a higher velocity. From the velocity plots, it can be seen that the highest velocity is seen at the center of the arrow.

From the concept of the boundary layer, as velocity increases, the flow transitions form laminar to turbulent. This transition point occurs when the Reynold's number is equal to 5×10^5.

$$Re_{\text{x}_\text{c}} = \frac{\rho U_\infty x_c}{\mu} = 5 \times 10^5 \tag{31}$$

Using Equation 31, the transition point (x_c) along the arrows surface can be calculated. Using Table A.4 [9] for the density and viscosity values for air at 300K.

$$x_c = \frac{(5 \times 10^5)\mu}{\rho U_\infty} = \frac{(5 \times 10^5)(184.6 \times 10^{-7} \frac{Ns}{m^2})}{(1.1614 \frac{kg}{m^3})(30 \frac{m}{s})} = 0.2649m \tag{32}$$

At 0.2649 m from the end of the arrow head, it is expected that the flow will transition from laminar to turbulent flow. From Figure 48, when accounting for the x-axis shift of -1, it can be seen that the turbulent flow region begins at around the -0.75 point. From this point onward, an increase in velocity is seen along the surface of the arrow [**?**].

6.2   Comparison Between Behaviors Around Different Fin Type

6.2.1   Geometry Impact on the Flow around the Fin

The major difference between each fin design is the preceding section and trailing section of the fin. To be more specific, the figure below shows which section of the arrow differs for each fin type.
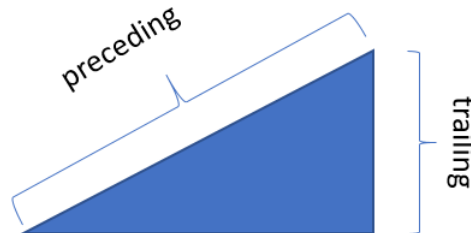

Figure 49: Fin Section Label

As seen from the Results section, the design of the fin (as shown above), will determine how the flow behaves around the fin and how much drag force the arrow will experience overall. Starting with the Old English KL fin type, this is one of the most used fins in the archery sport. The preceding and trailing sections of the fin is modeled based on the linear profile. This modeling method allows the flow to be uniformly distributed on the preceding section of the arrow, while maintaining a low wake region at the tail of the arrow (as seen in Figure 20) and minimum shear stress acting on the surface. On the other hand, Old English SL has quite a similar design to the Old English KL. The main difference is that the preceding and trailing section of the arrow fin for this type is modeled to be following a curve. This introduces a much larger wake region at the end. This is seen to be less stable and might potentially create some non-predicted behavior for the flow around the arrow, leading to much large drag on the arrow itself. Pope and Young fin type has the similar design concept compared to old English KL, however, instead of fully linear modelling for the preceding section, the design also includes a small flat section in that area as can be seen in Figure 7. It is believed that this flat sector will introduce some drag effects from shear pressure which will result in slightly larger drag on the fin itself compared to the the Old English KL.

Regarding the model of the Shield Fin type, it can be seen from Figure 36 that the model is not quite accurate compared to the expectation in Figure 7. Even though the MATLAB set up for geometric profile produces stable results for the other fin types, when it comes to the Shield profile, the model becomes extremely unstable, and produces oscillation and a huge wake region at the end of the arrow. This does not match with the requirement, therefore, it can be reasoned that this model should be neglected as it proves to be unstable compared to the other fin types.

Lastly, the French Curve fin type shows the most promises feature due to both preceding and trail section of the arrow is modelled linearly; the difference between this and old English KL is that the trailing section is straight down to the arrow body, while the trailing section for the arrow is diagonally linear. By introducing this into the design, the flow will have a much smoother transition between the fin and the tail. Therefore, it is expected to have much smaller wake region and less drag forces acting on it overall.

6.2.2 Geometry Impact on Performance of Arrow

From simulated data as shown in Table 1, it can be seen that the lift and drag coefficient for all the fin types are approximately equal to each other. Ideally, in the archery sport, the arrow movement should have limited drag force and lifting force on the surface. In this study, it is assumed that there is no other force exerted (including weight) on the arrow except for the incoming uniform flow such that it allows the arrow to travel as straight as possible to the target. Therefore, the ideal arrow should have the minimal drag coefficient and lift coefficient. As a result, from Table 1, with the exception of Shield fin type, it can be seen that Old English KL is proved to be the best according to simulation data with the drag coefficient and lift coefficient, 10.84 and -0.27, respectively.

From the perspective of stability of the arrow, it will be judged based on the momentum coefficient at the center of the arrow. Ideally, to have the arrow flying straight to the target, there should be minimal momentum at the center. After examining the moment coefficient, by compensating for the effect of the drag and lift coefficient on the arrow, the Old English KL fin type is considered on the the best overall as its moment coefficient to be 0.24 even though the lowest moment coefficient belongs to Shield fin type.

6.3 Angle of Attack Effect of Performance of Arrow

Previously in the result, the simulations were done using an angle of attack of 0 degrees. Since the best geometry of the fin is identified in previous section was the Old English KL, the following section will focus on what is the appropriate angle of attack for the arrow to be stable. This will be evaluated based on the pressure distribution along the arrow surface and the moment coefficient at the center of the arrow that determines the stability margin. Three angles of the attacked will be considered in this study: 0 degrees, 3 degrees and 7 degrees. Please note that 7 degrees is the maximum angle of the numerical model can achieve as any angle larger than 7 degrees will result in the model collapsing on itself. It is suspected that the model that is currently set up is not able to model stalling else there could be an error when running the model. Therefore, 7 degree is the limitation of the running model. The following table shows the calculated values for varying angles of attack.

	0 Degrees	3 Degrees	7 Degrees
Arrow Tip Moment (N×M)	-8.36 $\times 10^3$	1.08 $\times 10^6$	1.16 $\times 10^6$
Drag (N)	4.71 $\times 10^4$	2.36 $\times 10^4$	-1.07 $\times 10^4$
Drag Coefficient	10.84	5.08	-2.31
Lift (N)	-1.16 $\times 10^3$	1.5 $\times 10^5$	1.97 $\times 10^5$
Lift Coefficient	-0.27	32.53	42.33
Moment Coefficient	-0.24	26.91	29.07
Static Margin	0.40	0.32	0.20

Table 2: Flow Properties for Differing Old English KL Angle of Attacks

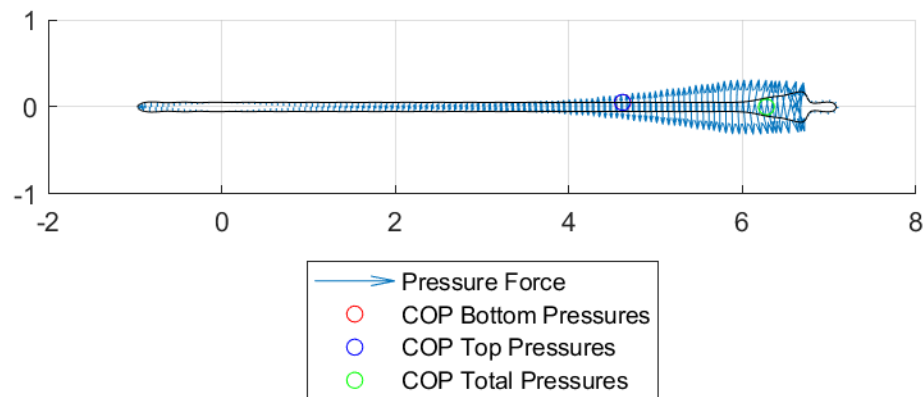The following figure shows the angle of attack of 0 degrees:

Figure 50: Arrow Surface Pressure Distribution with Center of Pressure with 0 Degree

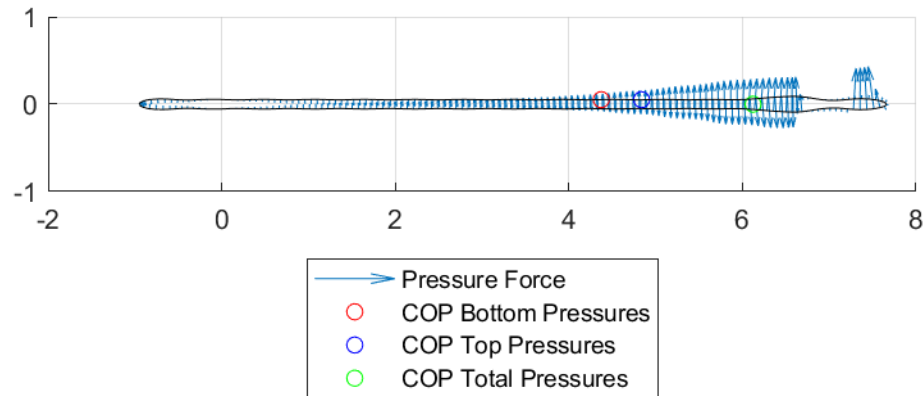The following figure will show the angle of attack of 3 degrees:

Figure 51: Arrow Surface Pressure Distribution with Center of Pressure with 3 Degree

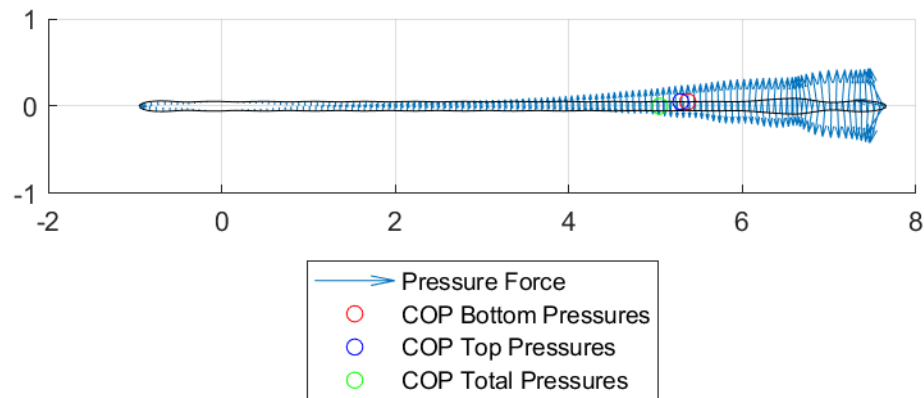The following figure will show the angle of attack of 7 degrees:

Figure 52: Arrow Surface Pressure Distribution with Center of Pressure with 7 Degree

At the angle of attack of 0 degrees, it is shown that the lift coefficient and corresponding lift force is approximately 0. It is also shown that as the angle of attack increases to 3 degrees and 7 degrees, the lift coefficient increases to a value of 32.53 and 42.33, respectively as expected according to [?, pg.613]. This can be explained as the attack of angle increases, the surface at the bottom of the arrow experiences much higher pressure which introduces negative pressure gradient from the bottom to the top surface. This will result in lift acting on the surface on the arrow. On the other hand, when examining the drag coefficient, it gradually decreases as the angle increases, which is unexpected. Typically, when the angle of attack increases, due to much high surface area for the incoming flow interacting with the surface, this should increase the drag coefficient. This can be only concluded that there is some insignificant unresolved issues in the models itself such that it allows to generate negative drag. However, this result does not alter the credibility of any other analysis mentioned before. Subsequently, to analyze for the stability of the arrow, as discussed before, the moment coefficient will be used to argue. As can be seen from Table 2, the moment coefficient of angle 0, 3, and 7 degrees result to the following moment coefficients, -0.24, 26.91 and 29.07, respectively. Therefore, since the angle attack 0 degree results lowest moment coefficient, this angle is concluded to the most stable flow.

From the pressure plot perspective, as observed Figure 50 and Figure 52, with the angle increase 7, the pressure distribution shift to the tail of the arrow. This is not ideal for the arrow since if there is uneven

pressure distribution on the arrow, this will cause the flow of arrow to become unstable and unpredictable since it introduces a moment about the center of the arrow. Therefore, from both numerical solutions and plotting data, both concluded that the angle of attack of 0 degree will result in the most stable overall.

7   Conclusion

In conclusion, it was determined that the most stable fin geometry was the Old English KL. By analyzing the fin geometry, it was determined that the linear profile of the preceding and trailing sections of the Old English KL fin meant that the fluid was uniformly distributed on the preceding section. This resulted in a low wake region at the tail of the arrow. The geometry of the Old English KL fin meant that the fin experienced a lower drag coefficient and lift coefficient when compared with the other fin geometries.

To further analyze the affect of fin geometry on the stability of the arrow, simulations were run for the Old English KL fin model using an angle of attack of 0°, 3°, and 7°. It was determined that as the angle of attack increases, the drag and drag coefficient decreased while the lift and lift coefficient increased.

The most stable fin geometry is the Old English KL and the most stable angle of attack is 0 °.

8 References

[1] "Archery." [Online]. Available: https://olympics.com/en/sports/archery/

[2] "Will a shoulder brace for archery work for you? check this out." 2020. [Online]. Available: https://archerydude.com/will-a-shoulder-brace-for-archery-work-for-you/

[3] S. Yarusevych, "Lecture 7 notes," Learn, 2023, learn provided notes. [Online]. Available: https://learn.uwaterloo.ca/d2l/le/content/959258/viewContent/5090059/View

[4] ——, "Lecture 14 notes," Learn, 2023, learn provided notes. [Online]. Available: https://learn.uwaterloo.ca/d2l/le/content/959258/viewContent/5090068/View

[5] "Potential flow," 2023. [Online]. Available: https://potentialflow.com/

[6] F. White, *Fluid Mechanics*, 8th ed. New York, NY: McGraw-Hill Education, 2016.

[7] "Arrow 101," 2018. [Online]. Available: https://archery360.com/2018/11/28/arrows-101/

[8] "Various feather clipper blades," 2023. [Online]. Available: https://www.thelongbowshop.com/products/vario-feather-clipper-blades

[9] F. M. White and H. Xue, *Fluid Mechanics*, 9th ed. New York, NY: McGraw-Hill Education, 2021.

[10] A. Svirin, "Complex form of fourier series," Math24, 2016. [Online]. Available: https://math24.net/complex-form-fourier-series.html

[11] T. DeLillo, "Fourier series methods for numerical conformal mapping of smooth domains," Wichita State University Math Dept, 2014. [Online]. Available: